Tectonophysics 765 (2019) 52–63

Contents lists available at ScienceDirect

Tectonophysics

journal homepage: www.elsevier.com/locate/tecto

Impact of host rock heterogeneity on failure around pressurized conduits: Implications for finger-shaped magmatic intrusions

Alban Souche[a,*,1], Olivier Galland[a], Øystein Thordén Haug[a], Marcin Dabrowski[a,b]

[a] Physics of Geological Processes, The NJORD Center, Geosciences Department, University of Oslo, Norway
[b] Computational Geology Laboratory, Polish Geological Institute - National Research Institute, Wrocław, Poland

ARTICLE INFO

Keywords:
Pressurized conduits
Magmatic fingers
Heterogeneity
Shear failure
Elastoplasticity
Numerical modelling

ABSTRACT

Rock failure accommodating the emplacement of magmatic intrusions is controlled by the local stress regime within the host rock. Most of the mechanical models addressing rock failure conditions (e.g., for a given tectonic regime or magma overpressure) simplify the stress calculation by assuming the homogeneity of the host rock properties. In this study, we highlight the importance of local heterogeneities in controlling the localization of the deformation and the failure mechanism around a magmatic intrusion. We numerically model the elasto-plastic deformation of a heterogeneous host rock intruded by an overpressurized magmatic body of cylindrical or finger-shaped geometry. The plastic component of the deformation is considered with a mixed mode mechanism allowing dilatant and shear displacements to act simultaneously. Our simulations are performed for small strain amplitudes that reflect the pre-failure conditions of the host. We assess the subsequent failure mechanism of the system based on the development of the localized strain patterns. The heterogeneity in the model is introduced by a stochastic perturbation of the host rock cohesion with characteristic wavelength and amplitude. We show that a relatively small perturbation of ± 10% of the cohesion field can efficiently localize the plastic deformation and control the subsequent emplacement mechanism. We further investigate a more realistic geological scenario in which the intrusion resides within sedimentary layers of contrasting strength, resulting in both heterogeneity and anisotropy of mechanical properties in the host rock. Our model reproduces similar deformation patterns as observed around finger-shaped magma intrusions within the Vaca Muerta shales in the Neuquén basin, Argentina. We conclude that heterogeneities within the host rock may locally "seed" dilatant shear faults around magmatic conduits and finger-shaped intrusions and result in the development of a process zone of length scale in order with the intrusion radius length scale.

1. Introduction

Magma transport in volcanic plumbing systems is a complex geological process characterised by a high degree of coupling between the flow of the magma and the deformation of the host rock (Galland et al., 2018; Keller et al., 2013; Lister and Kerr, 1991; Rivalta et al., 2015). The dynamics of the system is to a great extent governed by the mechanical response of the host from the forceful intrusion of magma. Unravelling the mechanical behaviour of the host rock is thus essential for understanding magma propagation through the crust and assessing the emplacement mechanism of the magma itself in the system. The deformation mechanism and structures associated with magma emplacement also have significant implications for geological processes affected by magmatism such as fluid flow around igneous intrusions emplaced in organic-rich sediments or aquifers (Chevallier et al., 2004; Senger et al., 2017; Rodriguez Monreal et al., 2009; Spacapan et al., 2018), and earthquake swarms preceding volcanic eruptions (Ágústsdóttir et al., 2016; Rubin and Gillard, 1998; White et al., 2011).

Most mechanical models of magma propagation within the shallow crust (few kilometres depth) rely on the mechanical framework of the Linear Elastic Fracture Mechanics (LEFM) (e.g., Bunger and Cruden, 2011; Lister and Kerr, 1991; Pollard, 1987; Pollard, 1973; Rubin, 1993, 1995; Sammis and Julian, 1987; Townsend et al., 2017). Within the LEFM framework, the magmatic intrusion is treated as an overpressurized fluid-filled crack propagating through an elastic host by tensile opening, in analogy to hydraulic fracturing (e.g., Detournay, 2016). LEFM models are well established to study the emplacement of sheet intrusions such as dykes, sills, and thin laccoliths in the brittle

* Corresponding author.
E-mail address: alban@simula.no (A. Souche).
[1] Present address: Computational Physiology, Simula Research Laboratory, Lysaker, Norway.

https://doi.org/10.1016/j.tecto.2019.05.016
Received 16 September 2018; Received in revised form 12 May 2019; Accepted 22 May 2019
Available online 24 May 2019

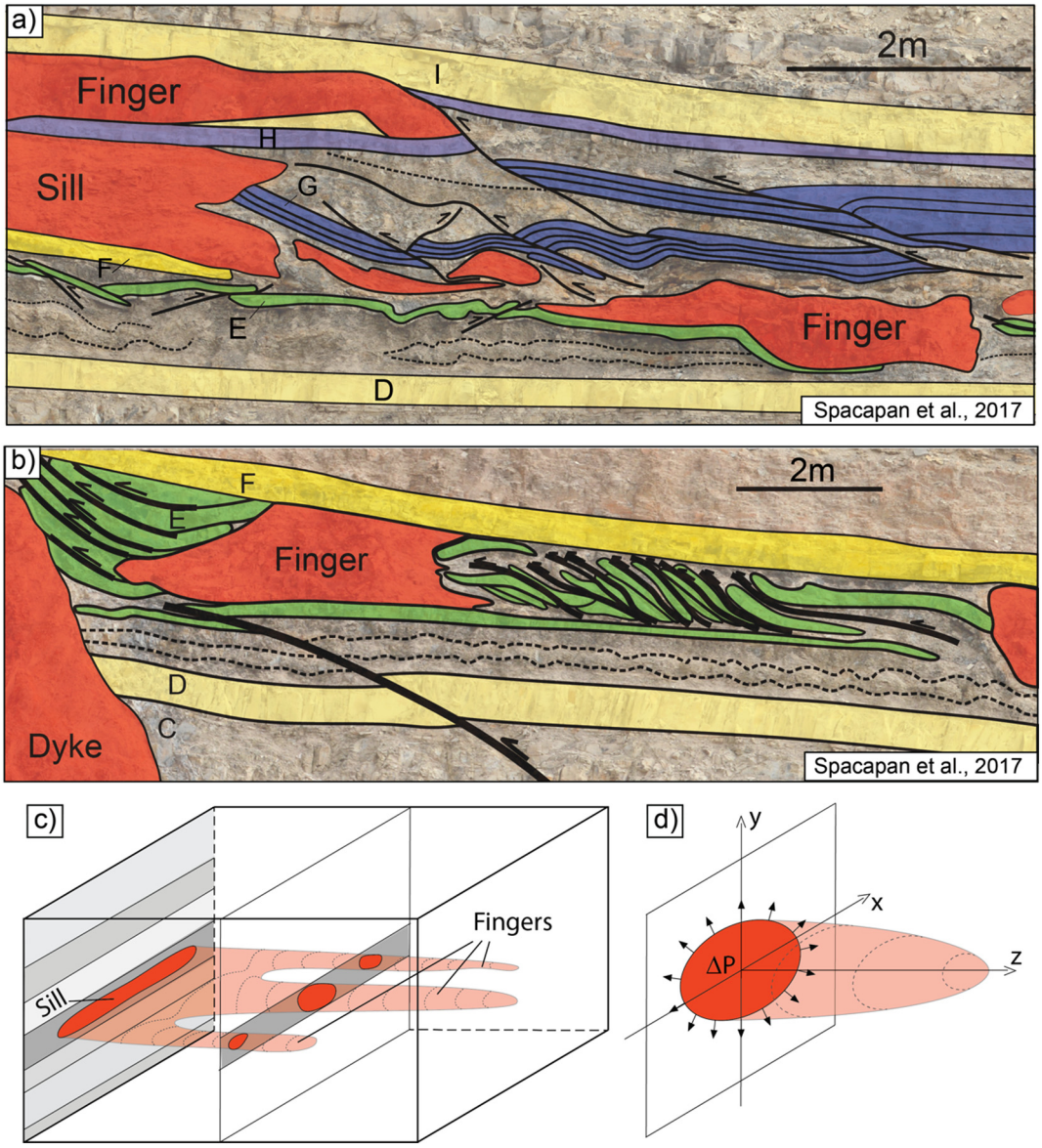

Fig. 1. a-b) (Modified from Spacapan et al. (2017)) Structural features associated with magmatic intrusions emplaced in the layered sediments of the Vaca Muerta Formation, Neuquén Basin, Argentina. Outcrop photograph in the background. The sedimentary layers (named with capital letters) are made of siltstones, shales and calcareous deposits. We refer to Spacapan et al. (2017) for details on the geological observations. c) Idealised geometry of sill and finger intrusions in a stack of sedimentary layers. d) Model setups plane (cross-section (x-y)) where the magma overpressure ΔP acting on the host is assumed constant.

crust (Kavanagh et al., 2006; Maccaferri et al., 2011; Michaut, 2011; Scheibert et al., 2017; Sigmundsson et al., 2015). Several assumptions are inherent to LEFM theory, including that the mechanical properties of the host rock are homogeneous, and that the process zone ahead of the intrusion tip is negligible in size. The last assumption may only be valid for sheet intrusions with large enough length-to-thickness aspect ratio (Pollard, 1973; Rubin, 1993; Scheibert et al., 2017) but may not apply to cylindrical volcanic conduits and specific igneous fingers in sedimentary basins (Fig. 1), which exhibit much smaller length-to-thickness aspect ratios (e.g., Pollard et al., 1975; Galland et al., 2019).

While the LEFM theory seems to provide sound predictions of the mechanical development of sheet intrusions, some geological and geophysical observations are however inconsistent with inherent assumptions of LEFM. Johnson and Pollard (1973), Pollard et al. (1975), Schofield et al. (2010) provided structural field evidence that the host rock deformation accommodating the emplacement of igneous fingers may occur dominantly in shear failure, which can extend over domains as large as the fingers themselves. This is observed particularly in the shale sequences of the Vaca Muerta in the Neuquén basin, Argentina, where igneous fingers were emplaced by intense shortening of their host rock, leading to rock wedging and imbricate stacks (Fig. 1, Spacapan et al., 2017; Galland et al., 2019). Pollard et al. (1975), Magee et al. (2017) and Galland et al. (2019), among others, also show that sheet intrusions such as sills are likely the result of coalescing aligned igneous fingers, suggesting that the emplacement of sheet intrusions cannot only be addressed by the LEFM theory. These studies show that revealing the complex inelastic deformation accommodating the growth and propagation of igneous fingers is thus essential to understanding the dynamics of large parts of volcanic plumbing systems.

Several studies attempted to consider the complex deformation within the host rock process zones (i.e., Pollard and Johnson, 1973; Pollard et al., 1975; Rubin, 1993). Instead of interpreting the principal stress trajectories in terms of tensile failure, these authors inferred that shear failure can occur along the planes of maximum shear stress near the tips of overpressurized intrusions. These models, however, only treated purely homogeneous and isotropic host rock. Conversely, Rubin

and Gillard (1998) showed that a few pre-existing discrete fractures can substantially affect the mechanical response of the host near a dyke tip region, likely leading to fault slip reactivation or shear failure. With this relatively simple theoretical consideration, Rubin and Gillard (1998) highlighted the fundamental impact of host rock heterogeneity (via discrete discontinuities) on the failure mechanism of the host. Given that rocks in nature are heterogeneous and often anisotropic, the results of Rubin and Gillard (1998) suggest that considering the natural rock heterogeneity is critical in assessing the failure mechanism within outcrop scale process zone.

None of the models listed above are actually able to assess the evolution of the inelastic deformation of the host. Different models using elastoplastic rheology (Currenti and Williams, 2014; Gerbault et al., 2012; Gerbault et al., 2018; Minakov et al., 2018), damage theory (Carrier et al., 2015; Got et al., 2017; Mériaux et al., 1999; Got et al., 2019), or limit analysis (Haug et al., 2018; Haug et al., 2017), have been explored to characterise the inelastic deformation patterns in the overburden of magma chambers and sills complexes. In these approaches, the modelled localized inelastic deformation is often interpreted as fault zones and, eventually, as magma pathways. With the exception of Minakov et al. (2018), the role of rock heterogeneity has received only little consideration in these numerical studies.

Our study focuses on the outcrop scale (meter scale) processes and aim to provide a mechanical model to account for the shear deformation observed in the host rock near finger-shaped intrusions as described in the Neuquén basin (Fig. 1; Spacapan et al., 2017; Galland et al., 2019). To this end, we numerically model the development of inelastic deformation patterns in the process zone of a pressurized cylindrical intrusion model using the framework of elastoplasticity. We further highlight the implications of our results to motivate future research in understanding shear deformation mechanism associated with the emplacement of tabular magmatic intrusions, such as dykes and sills.

2. Setup and method

2.1. Setup

In all the models, the setup consists of a discrete and static interface between an overpressurized magmatic intrusion and the host rock. The plane of study can be envisioned as a circumferential cross section through a horizontal magmatic finger (Fig. 1 c and d) with a radius of 1 m. The aim of the simulations is to quantify the elastoplastic deformation of the host rock as a result of constant pressure increase along the interface. The pressure is applied by incremental loads, and for each increment, a corresponding elastic or elastoplastic deformation is calculated and cumulatively added to the total deformation field of the host rock. The strain amplitude explored in our study lies in a range of 10^{-3} to 10^{-2}, which are typical measured values in triaxial experiments before macroscopic failure collapse of sedimentary rocks (Ambrose, 2014). We therefore model the pre-failure deformation and the development of the process zone in the system. In addition, we assume the plastic deformation to be associated with a dilatant volumetric change of the host, which is also a measured behaviour of many rock types in pre-failure conditions (Ambrose, 2014; Baud et al., 2000). Any subsequent failure mechanism can be interpreted from the modelled strain and stress fields.

We first perform a systematic study of the elastoplastic deformation pattern around an 2D pressurized circular cavity (*Model 1*, Fig. 2a). The motivation behind the geometry of *Model 1* is to establish a reference framework where the focus is given to systematically quantify the impact of the heterogeneity. The calculations presented with the *Model 1* neglect the gravity term in the pressure equation, which directly implies a lithostatic pore fluid pressure through the host (e.g. Gerbault et al., 2012; Grosfils et al., 2015), and indirectly favour tensile failure condition by reducing the deviatoric stress in the system. We take advantage of this end-member stress scenario in *Model 1* to be conservative in the quantification of shear deformation.

We then perform a series of simulations with a more realistic geological setup (*Model 2*, Fig. 2b) reflecting the emplacement of a horizontal, flatten finger intrusion (Fig. 1d) into a stack of sedimentary layers of different cohesions. The finger is assumed to be emplaced at a depth of 1 km. Two scenarios without and with full gravitational loading are presented in *Model 2*. This allows us to cover two end-members for the host pore fluid pressure, which has shown to be of importance for the strain development around larger magmatic systems (Gerbault et al., 2012; Grosfils et al., 2015). In addition, the gravitational loading is implemented as a lithostatic stress with equal stresses in all directions, as opposed to a uniaxial strain loading (see, e.g., Grosfils (2007) for further discussions on the topic).

It is important to note that the boundary conditions along the top and right walls of *Model 1* and *Model 2* are set sufficiently far away from the model intrusion to not affect the numerical results. For completeness regarding the implication of the boundary conditions used in our study, we refer to the Supplementary Material.

2.2. Heterogeneity

Rock heterogeneity can span over several orders of magnitude in characteristic length scale (mm to km) and can exhibit a large variety of patterns reflecting, for instance, the layering and lithological variations in sedimentary basins, the existence of fault network in areas affected by tectonics, or, to a smaller scale, porosity. Layers represent a first-order mechanical heterogeneity within sedimentary basins with cohesion contrasts within, at least, one order of magnitude (Schellart, 2000). This is exemplified in Fig. 1, where “soft” silts and shales layers alternate within “strong” calcareous layers. In addition to being heterogeneous, rocks such as shales are also mechanically anisotropic. In this study, we implement both the effects of rock heterogeneity and anisotropy with isotropic and anisotropic distributions of the cohesion field.

In *Model 1*, we generate an isotropic stochastic noise that we use to perturb the cohesion field of the system. With this definition, the heterogeneity acts as a weakness (or strength) in our model by locally shifting the onset of plastic yielding to lesser (or greater) deviatoric stress conditions. The perturbation is generated as a stochastic field with spectral properties corresponding to a self-affine distribution with Hurst exponent 1 and limited by an upper cut-off wavelength (Fig. 3 a and b). The cut-off wavelength determines the spectral range of the self-affine scaling of the perturbation, giving rise to the pattern presented in Fig. 3 c-f. We will refer to the cut-off wavelength as the characteristic wavelength of the heterogeneity in the following sections of the paper.

Anisotropic perturbation fields in *Model 2* are generated in the same way as the isotropic fields but are stretched with a given factor in a preferential direction (laterally in our applied geological scenario *Model 2*). This type of perturbation is used to reflect stratigraphic variations within individual sedimentary layers and to a certain degree rock anisotropy.

One important aspect when considering small characteristic wavelength of the heterogeneity is to accurately discretize it on the numerical mesh. To avoid any sampling bias in this process, we increase the space discretization when exploring perturbations with relatively small wavelength (λ_c), with mesh resolution ranging from ~2e6 to ~20e6 nodes.

2.3. Elastoplastic framework and numerical tool

The numerical simulations presented in this paper have been performed using a 2D finite element model, implementing compressible Drucker-Prager elastoplasticity within the small strain approximation. The code is written in MATLAB and freely available from the OpenGeoNabla suite (Souche, 2018), where the scripts and benchmarks are accessible from the GitHub project repository.

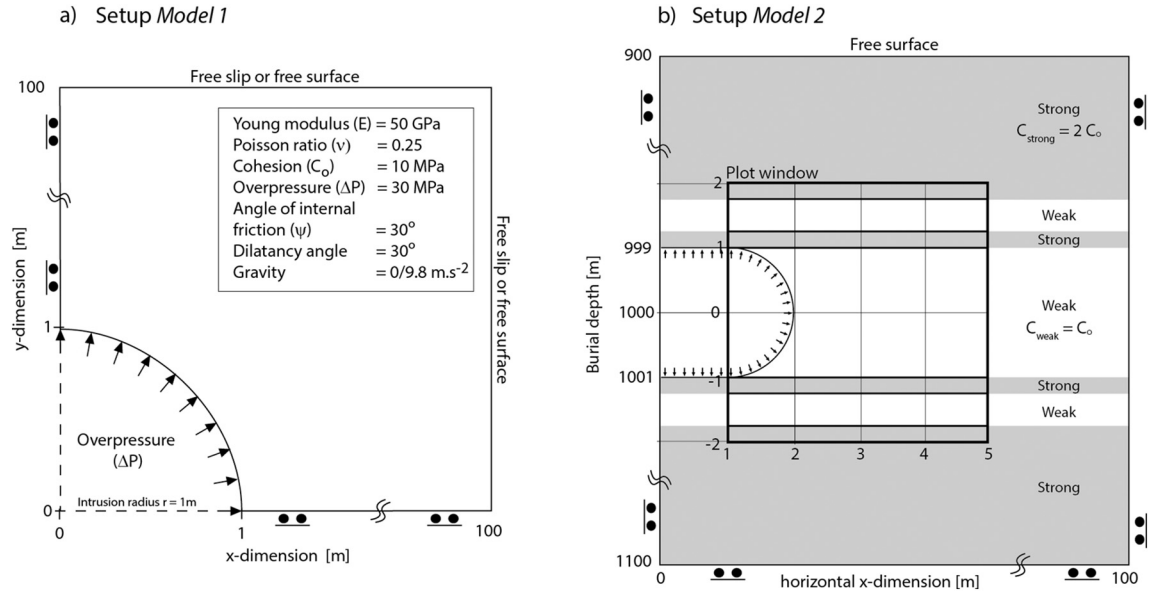

Fig. 2. a) Geometry and boundary conditions used in the *Model 1* and *Model 2*. Note that the total extent of the domain is 100 times the intrusion radius (set to 1 m in both experiments). As 2D plain strain representation, *Model 1* setup approximate an infinite cylinder geometry and *Model 2* approximate a finger-shaped intrusion with a plane of symmetry formed by the vertical and out-of-plane axis. Both setups can be envisioned as circumferential cross-sections through a horizontal finger intrusion (Fig. 1 c and d).

The transition between the elastic and the elastoplastic deformation is approximated by a Drucker-Prager yield function (F). F is negative in the elastic domain and positive in the elastoplastic domain, following the expression:

$$F = \sqrt{J_2} + \eta P - \varepsilon C, \tag{1}$$

where C is the rock cohesion, J_2 is the second invariant of the deviatoric stress tensor, P is the pressure, and η and ε are expressed as functions of the angle of internal friction ϕ (de Souza Neto et al., 2011):

$$\eta = \frac{3\tan\phi}{\sqrt{9 + 12\,tan^2\phi}}, \quad \varepsilon = \frac{3}{\sqrt{9 + 12\,tan^2\phi}}. \tag{2}$$

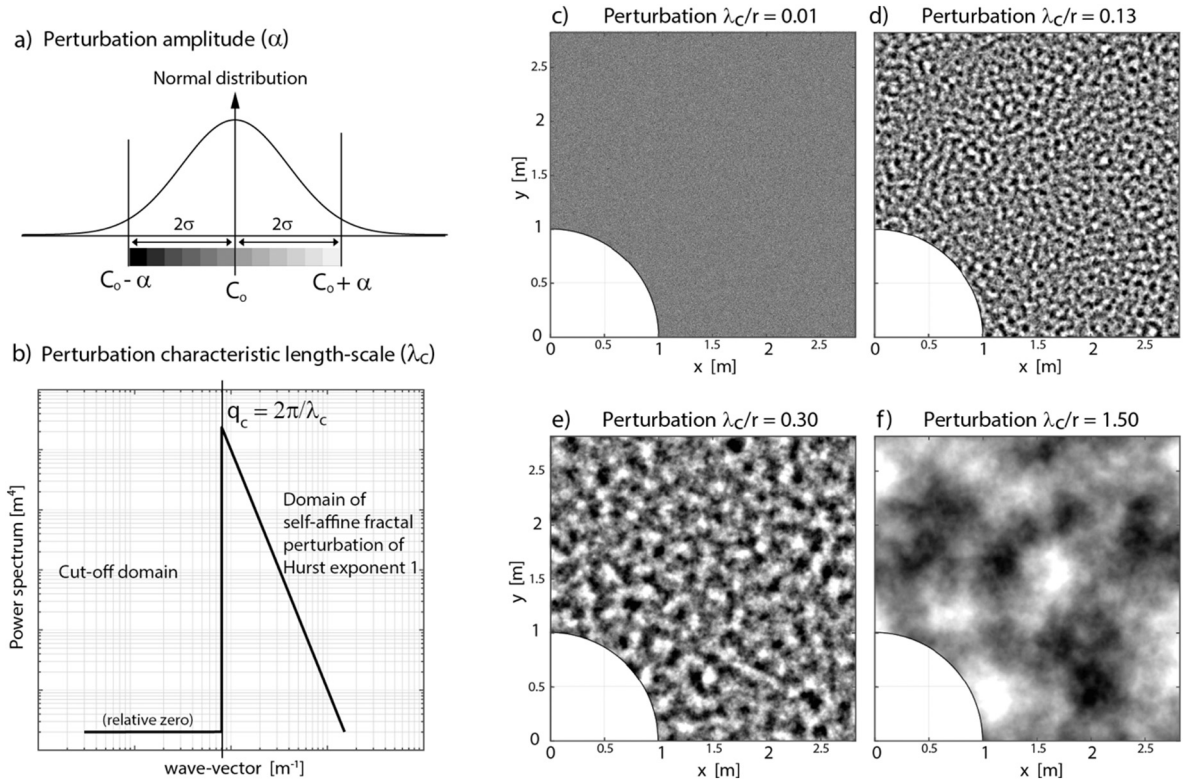

Fig. 3. a) Normal distribution of the cohesion with a perturbation amplitude (α) defined as 2 standard deviations (2σ). b) Power spectrum of the fractal perturbation model (with Hurst exponent of 1) characterised by a cut-off wave-vector (q_c) used to set the desired characteristic wavelength (λ_c) of the heterogeneity in the model scenarios. c-f) *Model 1* perturbation field for 4 different values of the characteristic wavelength set respectively to 0.01, 0.13, 0.75, and 2 times the intrusion radius r.

The plastic deformation is associated with dilatant opening of the host, that we implemented by using an associative plastic flow rule. This assumption results in an angle of dilatancy equal to the angle of internal friction of the rock (set to 30°).

The non-linearity of the elastoplastic deformation is solved using a Newton-Raphson algorithm with a consistent tangent operator (Adamuszek et al., 2016; de Souza Neto et al., 2011; Yarushina et al., 2010). The solver is characterised by a quadratic convergence to the solution, with relative residual ($< 10^{-10}$) reached in usually < 10 iterations. The assembly and factorisation of the linearized system of equations is efficiently performed using the MILAMIN solver approach (Dabrowski et al., 2008). Further computational efficiency is obtained from the advantageous implementation of the associative plastic flow rule (de Souza Neto et al., 2011), which enables us to perform high resolution models required to resolve the prescribed level of material heterogeneity.

3. Results

3.1. Model 1: homogeneous and isotropically heterogeneous host

The plastic strain fields obtained in the homogeneous case (with constant rock cohesion, Fig. 4a) and heterogeneous case (with perturbed cohesion field, Fig. 4b) show remarkable differences depending on the perturbation introduced in the system. These differences are also well illustrated on local displacement fields (Fig. 4 e and f). The stress fields are used to assess the subsequent failure mechanism and are presented using principal and shear stress trajectories (Fig. 4c and d), and as Mohr circles for selected points near the intrusion (Fig. 4g and h.

In the homogeneous case, we observe the development of an axially symmetric strain profile consequent to the pressurization of the intrusion, with a plastic front progressing away from the intrusion interface. We observe that the largest principal stress is radial to the intrusion interface, and that the least principal stress is concentric, as well as the plastic front. In order to visualize the displacement field, we plot the displacement vectors at a given distance from an arbitrarily selected radial segment (black line with red dots in Fig. 4 a and e). We observed that the displacements are divergent and normal with almost no tangential components on both side of the segment, showing clear dilatant opening of the system (Fig. 4e). The stress state at point P1 is presented in Fig. 4g at different stages during the pressurization of the intrusion. We observe that for loads below 15 MPa, the Mohr circles intersect a critical stress region in tension (red triangle in Fig. 4g) defined by the apex of the yield envelop and the Griffith tensile criteria (here, Co/2 = 5 MPa). It can be argued that the use of a Mohr-Coulomb envelop (approximated by Drucker-Prager in the calculations) may not well approximate the early stage of the plastic yielding in this case, but it has a minor importance on the evolution of the system since it is associated with strains ($< < 10^{-3}$) much smaller that the failure criteria. Loading from 15 to 30 MPa result in a shift of the Mohr circles towards compressive stress regime where shear failure is expected. We idealise the failure conditions by a blue star along the 30 MPa loading Mohr circle, for which the modelled plastic strains might reach the limit of failure initiation.

In the heterogeneous case (Fig. 4), the isotropic stochastic perturbation of the cohesive field has a characteristic wavelength of 0.30 m and an amplitude of ± 10%. All the deformation of the host develops and localizes within an eccentric pattern reflecting the orientation of the shear stress trajectories, as shown in Fig. 4c. Displacements are given along a selected plastic strain zone (black line with red dots in Fig. 4 b and f). We observe a divergent displacement field from the referent middle segment with both normal and tangential components, showing a hybrid dilatant-shear opening (Fig. 4f). The Mohr diagram (Fig. 4h) showing the stress conditions at point P1 during loading is identical to the homogeneous case with the exception of a slight shift of the yield and the Mohr circles. This shift is induced by a locally lower cohesion.

In both the homogeneous and heterogeneous models, we define the plastic front (solid line and dash line in Fig. 4 a and b) as the maximum extent of the inelastic deformation. The positions of the plastic front in the homogenous and heterogeneous models are very similar. In addition, Fig. 4 c and d display the principal and shear stress trajectories of both simulations. We notice that even if the plastic strains strongly differ between the homogeneous and heterogeneous models, the stresses remain almost identical.

3.1.1. Effect of the characteristic wavelength of the heterogeneous cohesion field

We performed a series of simulations varying systematically the characteristic wavelength of the heterogeneity from 10 mm to 2 m, corresponding to a ratio λ_c/r of 0.001 to 2. Since each simulation result reflects the stochastic nature of the introduced heterogeneity, we repeated each experiment 15 times (270 simulations in total) to produce statistically relevant results to analyse. Note that the scaling factor "r", corresponding to the intrusion radius, is introduced in order to normalize the characteristic wavelength of the heterogeneity to a simple length scale of the system. We do not suggest, here, to apply the results to any scale given the simplification made in our model on regional scale processes (no tectonic stress, no interplay with potential magmatic reservoirs, etc.). Our results best apply to the outcrop-scale, highly sensitive, as we show, to local heterogeneities.

In Fig. 5a-d, we display the difference between the second invariant of the deviatoric strain tensor from the perturbed model with heterogeneous cohesions $(\varepsilon_{II}^{pl})^{pert}$ and the model with homogeneous cohesion $(\varepsilon_{II}^{pl})^{h}$. We observe distinct shear band patterns with different characteristic wavelength of the perturbation (shown in Fig. 3 c-f, respectively). Bands of positive (negative) values of $(\varepsilon_{II}^{pl})^{pert}$ - $(\varepsilon_{II}^{pl})^{h}$ represent larger (smaller) plastic deformation than in the homogeneous model. Qualitatively, the maximum values of $(\varepsilon_{II}^{pl})^{pert}$ - $(\varepsilon_{II}^{pl})^{h}$ are higher in the models with perturbation wavelengths of $\lambda_c/r = 0.13$ and $\lambda_c/r = 0.3$ (Fig. 5b and c) than those with perturbation wavelengths of $\lambda_c/r = 0.01$ and $\lambda_c/r = 1.5$, which suggests a higher degree of plastic localization.

To analyse the plastic deformation in a quantitative and systematic manner, we consider the plastic strain ratio $(\varepsilon_{II}^{pl})^{pert}/(\varepsilon_{II}^{pl})^{h}$ along selected profiles at fixed distance from the cavity/host rock interface (Profile A and B located in Fig. 5 a-d). From these profiles we extract the local maxima and minima and the range that comprises 95% of the signal above and below the homogeneous solution, corresponding to a plastic stain ratio above and below 1 (Fig. 5 e-f), respectively. Fig. 5 g and h display the maximum and minimum values of $(\varepsilon_{II}^{pl})^{pert}/(\varepsilon_{II}^{pl})^{h}$ along Profiles A and B as function of the perturbation wavelength for all the 270 simulations; the black curves represent the mean values of each investigated perturbation wavelength. The curves of Fig. 5g show the mean values of maximum (> 1) and minimum values (< 1) of $(\varepsilon_{II}^{pl})^{pert}/(\varepsilon_{II}^{pl})^{h}$ along Profile A. We observe that the maximum values (95%) have a positive bell shape reaching maximum around $\lambda_c/r \sim$ (0.05–0.1). The trend for the curve of the minimum values is not as clear but can be seen as an inverted bell shape. For perturbation wavelengths on both sides of the range 0.05–0.2 (5–20% of the intrusion radius), the plastic strain solution seems to approach progressively the reference homogeneous model strain solution.

3.1.2. Effect of the amplitude of the heterogeneity

Fig. 6 displays the mean values of the maxima and minima of $(\varepsilon_{II}^{pl})^{pert}/(\varepsilon_{II}^{pl})^{h}$, as defined in Fig. 5, as a function of the perturbation amplitude. We observe a monotonous increase of the plastic strain for increased value of the perturbation amplitude in the model, regardless of the considered profile (here, along Profile A and B). One important aspect to read from this plot is the relatively large impact induced by small amplitude perturbations on the localization of the plastic strain. For instance, a perturbation of ± 10% of the background cohesion will locally contribute to the development of shear bands with plastic strain

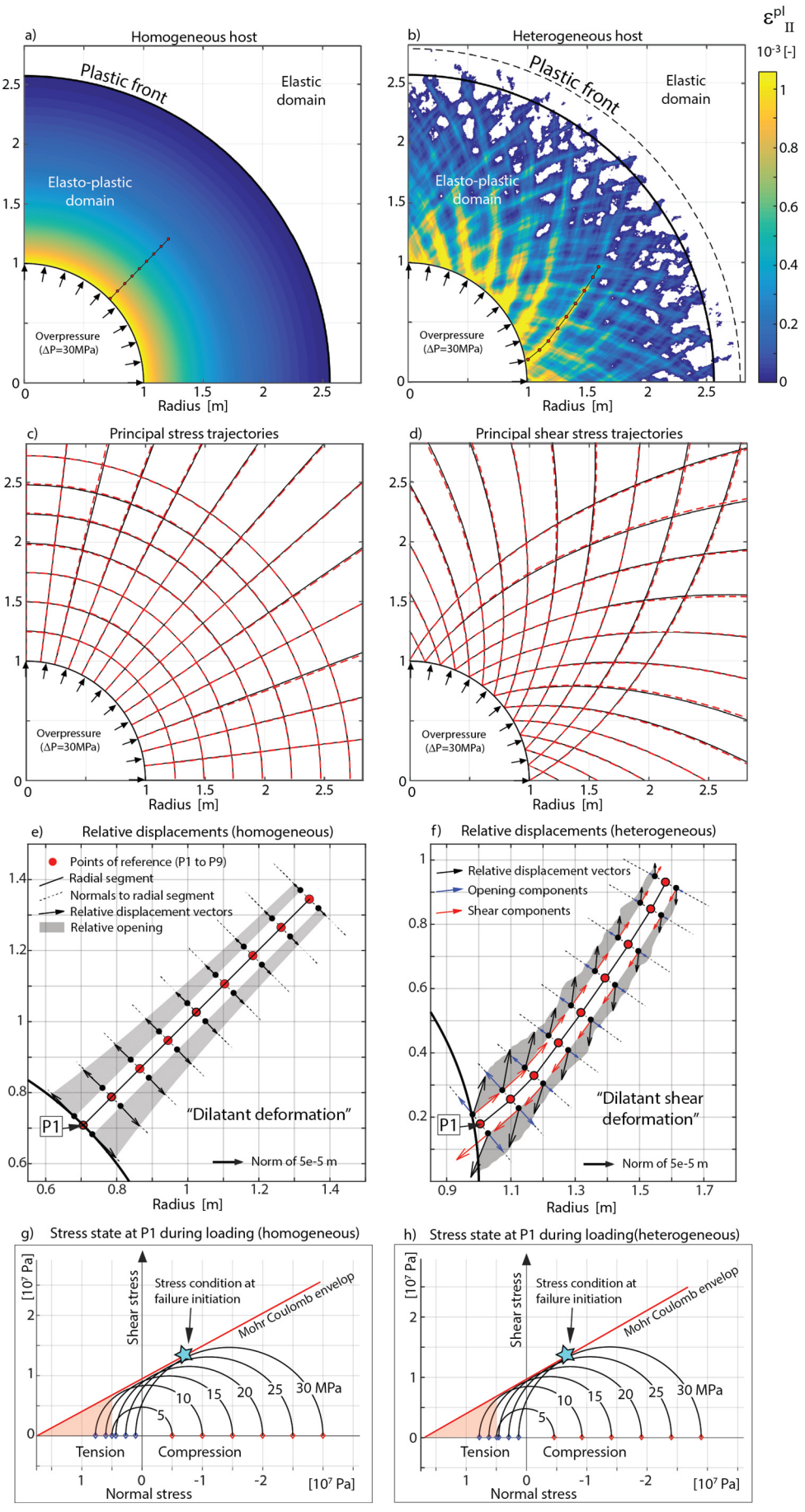

Fig. 4. Second invariant of the deviatoric plastic strain tensor in the a) homogeneous case scenario and b) heterogeneous case scenario (perturbation defined with λ_c = 0.30 m and α = ± 10%, Fig. 3e). Applied pressure of 30 MPa along the inner interface (See Fig. 2 for model setup and rock properties) and no gravitational loading. c) Principal stress trajectories and, d) maximum shear stress trajectories (black lines for the homogeneous model, red dash lines for the heterogeneous model). e-f) Displacement vectors calculated from reference segments (black line with red dots) chosen radially in the homogeneous model (a and e) and within a strain band in the heterogeneous model (b and f). The total displacement vectors are decomposed into opening and shear components for the heterogeneous model. g-h) Stress states in both model at points P1 during the incremental load of the intrusion (from 5 to 30 MPa). The blue stars represent the stress condition to consider for failure (shear failure in both cases) once the plastic strain become large enough. (For interpretation of the references to colour in this figure legend, the reader is referred to the web version of this article.)

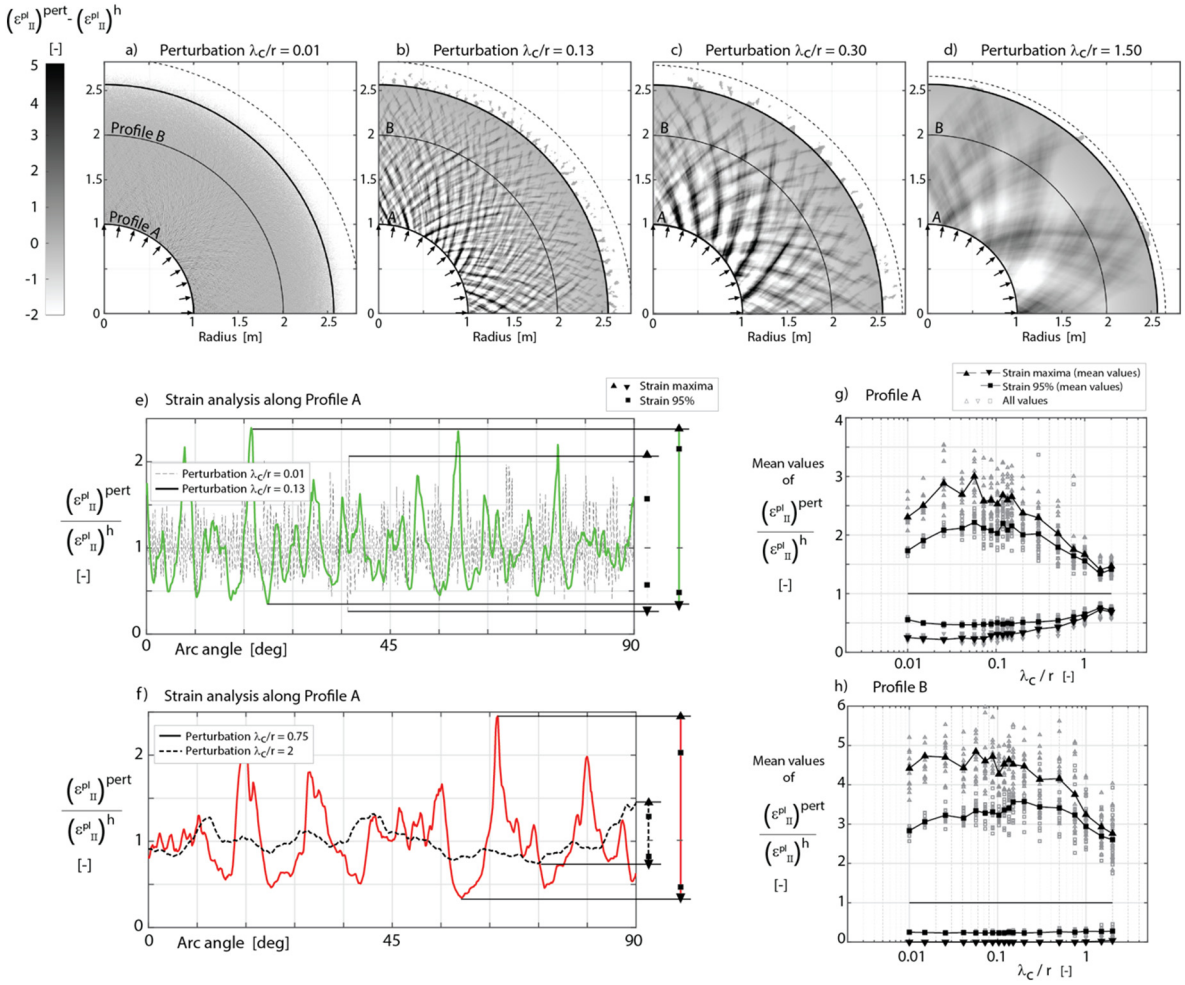

Fig. 5. a-d) Strain difference (second invariant of the deviatoric plastic strain) between heterogeneous models (Fig. 3 c-f, α = ± 10%) and the reference homogeneous model (Fig. 4a). e) and f) Plastic strain along Profile A normalized by the homogeneous solution (*right from the plot*: values of the maxima and minima (upper and lower triangles) and the value comprising 95% of the normalized plastic strain field (squares) below and above 1. g) and h) Mean values of the normalized plastic strain as function of the characteristic wavelength of the perturbation for Profile A and B over all the 270 experiments. The black lines represent the average value obtained for each investigated characteristic wavelength.

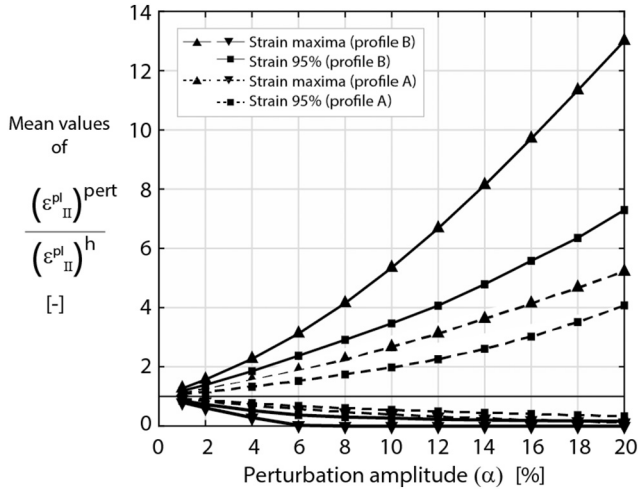

Fig. 6. Mean values of the normalized plastic strain maxima and minima along the Profile A and B (see Fig.5) as function of the perturbation amplitude (α).Perturbation set with λ_c = 0.15 m.

2 to 5 times greater than what would be expected from a homogeneous case scenario.

3.2. Model 2: layered and anisotropically heterogeneous host

We numerically assess two level of heterogeneity of the host in *Model 2*. The first level is represented by the presence of "weak" and "strong" layers. Their cohesions are defined with respect to the background cohesion C_0, such that $C_0^{weak} = C_0$ and $C_0^{strong} = 2C_0$. The second level of heterogeneity is introduced by adding an isotropic or anisotropic stochastic perturbation to the background cohesions (see Fig. 7 a-d). In addition, we evaluate the impact of gravitational loading in the model scenarios, by assuming either no gravity field (Fig. 7), which is equivalent as considering a lithostatic pore fluid pressure condition in the host, or including full gravitational loading (Fig. 8), which is equivalent as neglecting the role of pore fluid pressure in the confining pressure (Grosfils et al., 2015).

3.2.1. Model 2 without gravitational loading

In the model with no intrinsic layer heterogeneity, the plastic deformation develops along two localized shear bands that initiate from the intrusion and develop towards the upper and lower interfaces of the weak layer (Fig. 7 e). Some diffuse plastic deformation is also seen in the front of the intrusion and within the upper and lower weak layers

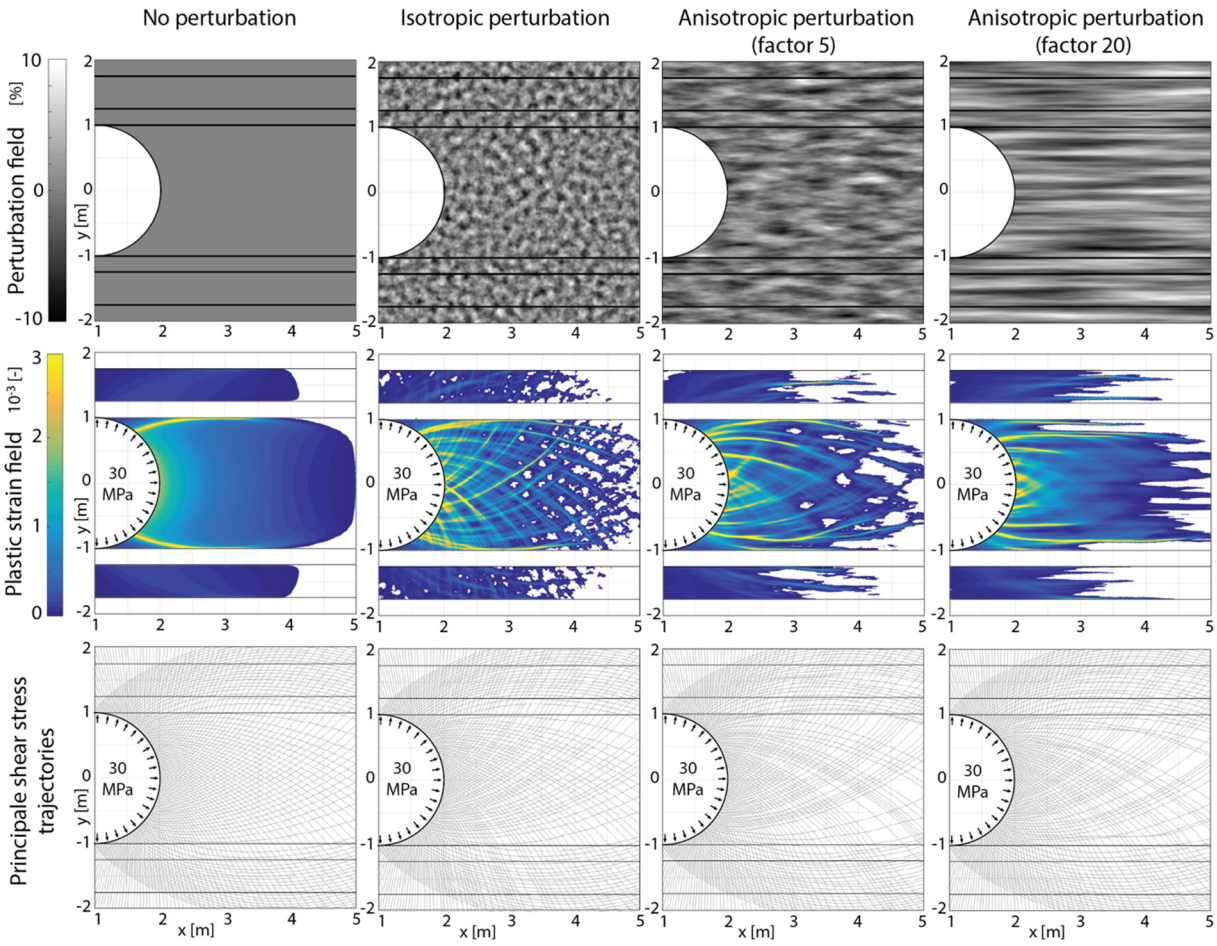

Fig. 7. Results of the layered *Model 2* without gravitational loading. (Top raw) Intrinsic perturbations applied to the cohesion field. "Strong" layers have a background cohesion of $C_o^{strong} = 2\ C_o$ and "weak" layers have a background cohesion of $C_o^{weak} = C_o$. (Middle raw) Corresponding plastic strain calculated for an applied pressure of 30 MPa along the intrusion. (Bottom raw) Corresponding principal shear stress trajectories.

beyond the strong layers. In this particular setup, the principal shear stress direction does not show strong deviation across the layers (Fig. 7i).

In the model with isotropic perturbation of layer cohesion, the plastic strain distribution in the weak layer is significantly different than in the model without perturbation. The main shear bands along the upper and lower interface of the intruded weak layer are still present, but other deformation bands of similar amplitude develop a conjugated shear band pattern, with an angle of ~60°.

Finally, the models with anisotropically distributed perturbation of layer cohesion (Fig. 7 c-d) result in the development of shear bands that tend to flatten in the orientation of the anisotropy (Fig. 7 g-h). This behaviour is also observed in the principal shear stress trajectories (Fig. 7 k-l), which in some cases seem to over cross. Increased anisotropy of the perturbation leads unambiguously to further flattening of the deformation pattern with the development of flat-lying shear bands within the intruded, but also non-intruded, "weak" layers of the model.

In all these model scenarios, a cohesion ratio of a factor 2 between the layers is enough to produce strong partitioning of the deformation, with almost no deformation within the strong layers. In addition, we observe that a perturbation of ± 10% significantly impact the development of the plastic strain pattern within the weak layers (intruded or not) of the model.

3.2.2. *Model 2 with full gravitational loading*

The results obtained with full gravitational loading (implemented as lithostatic stress) show a decrease of the plastic strain amplitude for a given magma overpressure (30 MPa, Fig. 8 a-d) in comparison to the equivalent scenarios without gravity (Fig. 7 e-h). Increasing the overpressure to 60 MPa, in our model, results in a plastic strain pattern that mirror the results obtained without gravity with 30 MPa overpressure. We observe that the region affected by the plastic deformation is restricted to a relatively smaller area, but the strain pattern remains relatively unchanged and is governed by the heterogeneity of the host.

4. Interpretation

In *Model 1*, there are striking differences in plastic strain patterns between simulations with and without heterogeneities (Fig. 4 a-b). In the homogeneous case, there is a radial zone of distributed plastic deformation, and the maximum and least stress trajectories are radial and concentric, respectively (Fig. 4 c-d). From the plot of displacements along a radial trajectory (Fig. 4 e), we clearly illustrate the dilatant opening of the host. A common interpretation at this stage would be to consider tensile failure radially emanating perpendicular to the least principal stress trajectories. However, the local stress regime along the interface shows compressional state that clearly suggests subsequent shear failure along other trajectories. As the strain field develops in a homogeneous and symmetric pattern, without localisation, it is not possible to further interpret the potential failure pattern in this case.

In the heterogeneous case, the stress conditions are almost identical as in the homogenous case, and local stresses along the interface clearly suggest shear failure of the system. It is straight forward, with the development of the localized plastic deformation parallel to the maximum

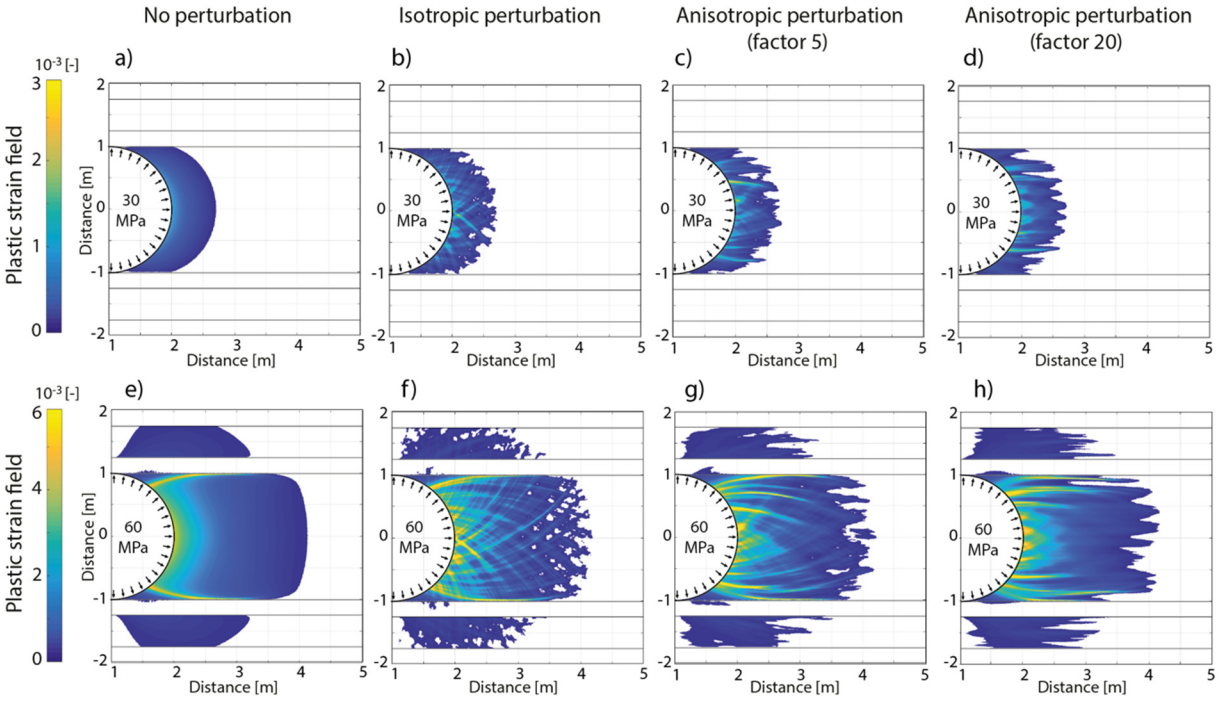

Fig. 8. Results with full gravitational loading end-member (assuming a confinement pressure equal to the overburden pressure at 1 km depth). The heterogeneity model used is identical to the one used in the model without gravitational loading (see Fig. 7 a-d). a-d) Plastic strain amplitude calculated with an applied magmatic overpressure of 30 MPa. e-h) Plastic strain amplitude with an applied overpressure of 60 MPa.

shear stress trajectories (Fig. 4d), to interpret the plastic strain pattern as representative for the subsequent failure pattern. By further interpreting the displacement field calculated within one of the shear bands (Fig. 4f), we show that dilatant opening of the host is compatible with localized shear fault development.

Fig. 5 shows how the amplitude of shear strain varies in heterogeneous models with respect to the perturbation wavelength: it shows that localization of the plastic deformation is maximal when $0.05 < \lambda_c/r < 0.2$, and it reduces for lower and higher values of λ_c/r. This result suggests that there is a preferential perturbation scale with respect to the scale of the system that favours plastic strain localization. If the perturbation is too small or too large, the system tends to behave closer to the homogeneous conditions. Several effects can lead to such behaviour: (1) For large λ_c, the probability of having a perturbation maxima or minima along the interface is statistically reduced and will restore, to some limits, a homogeneity of the host cohesion; (2) For small λ_c, the probability of finding a maxima or minima along the interface is high but, at the scale of the intrusion, the resulting deformation field tends to the deformation in a homogenous material; (3) For the smallest λ_c, a potential bias can be introduced when discretizing the perturbation field on a too coarse numerical mesh that does not fulfil the Nyquist sampling condition of the wavelength. We have carefully assessed this issue in our experiments and used refined numerical meshes for lower λ_c.

The localized deformation patterns at the close vicinity of the pressurized cavities extend to distances up to 1.5–2 m away from the intrusion radius (1 m), and we interpret this region as the process zone of the model. The extent of the plastic process zone in the homogeneous and heterogeneous simulations of *Model 1* are very similar, which suggests that subsequent failure development within the process zone would most likely extend to an equivalent radial distance from the interface for a given boundary load.

Our simulations show that small amplitude variations in the host rock properties have a strong impact on the development of distinct and contrasting strain patterns, by seeding and enhancing the localization of the deformation. The model with heterogeneity produces shear strains up to five times larger than those calculated in the homogeneous model (Fig. 5d), with a perturbation of only ± 10% of the host rock cohesion. The results, thus, highlight the significance of local rock heterogeneity, and provide valuable insights on assessing complex deformation patterns often seen around outcrop, i.e. meter-scale to x10 meter-scale, magmatic intrusions (e.g. Fig. 1).

In *Model 2*, the results highlight that (1) strata of contrasting cohesions and (2) anisotropic intra-layer heterogeneity such as in shale formations greatly channel and determine the plastic deformation induced by a pressurized finger-shaped intrusion. It shows how sedimentary layering strongly favours the layer-parallel propagation of igneous intrusions such as sills. In addition, even if each layers has homogeneous cohesion (Fig. 7a), the resulting plastic deformation occurs along localized dilatant shear bands. Our models thus suggest that layering and anisotropy strongly favour shear deformation associated with igneous intrusion propagation, as observed in the field (Spacapan et al., 2017).

The impact of the pore fluid pressure, assessed with the two end-member gravitational loadings, affects the amplitude of the modelled strain and the region of the process zone but has a little impact on the localization of the strain on the meter scale of our model. The finite amplitude of the modelled overpressure in the case of full gravitational loading (60 MPa) is potentially too high to be geologically relevant given the burial condition, and it should be interpreted as an upper estimate for the specific model parameters investigated. The absolute value of the overpressure could be lowered by reducing the rock cohesion in shallower crustal levels, for instance. However, our main interpretation of the results is that the local heterogeneity fully controls strain localization in our model.

5. Discussion

5.1. Importance of host rock heterogeneities

The Earth's brittle crust is naturally strongly heterogeneous at different scales, from submillimetre pore-scale to meter- and kilometre-

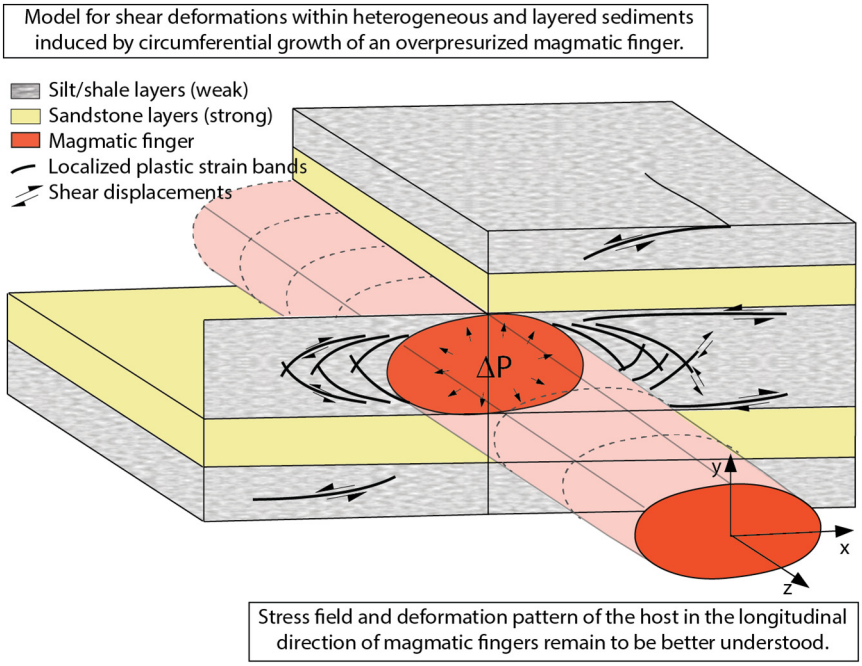

Fig. 9. Illustration of the model results and applicability to understand localized strain patterns in the circumferential cross-section of horizontal igneous fingers.

scale lithological variations, fractures, and faults. The heterogeneity introduced in our models, with a cohesion contrast between layers of factor 2 and a stochastic perturbation of amplitude ± 10% (Ambrose, 2014; Schellart, 2000), is within the lower range of natural rock variations, so the mechanical effects of layering and intrinsic cohesion fluctuations can be seen as realistic. Our models suggest that these natural heterogeneities control to a great extent the deformation of the brittle crust. Even if large scale deformation is not addressed in our models, we show that the failure mechanism within the process zone of the system may strongly be affected by the presence of heterogeneity, by seeding and enhancing the localization of the deformation (see Fig. 9).

While a large number of studies document the development of tensile opening in the emplacement of magmatic dykes and sills, the documentation of shear failure linked to the growth of magmatic intrusions has been sporadic. However, we can refer to the field observations of Johnson and Pollard (1973) and Spacapan et al. (2017) and Galland et al. (2019), who documented wedge-shape shear fracture network at the tip of sills emplaced in sedimentary rocks. Pollard and Johnson (1973) proposed a mechanical model of shear failure ahead of the intrusion, based on the analysis of the principal shear stress trajectories in an elastic host, to explain the observed eccentric shear fault pattern. Our results support this model and go further by (1) assessing the important role of host rock heterogeneities in developing such process zone and (2) modelling the development of plastic shear bands parallel to the principal shear stress trajectories. Our results are also in good agreement with sandbox models of magma intrusions, in which the model crust consist of granular materials that are heterogeneous by nature (Abdelmalak et al., 2012; Guldstrand et al., 2017). These experiments simulated the emplacement of dykes, the propagation of which was greatly controlled by shear failure of the heterogeneous host material.

5.2. Stress analysis versus plastic strain modelling

Dyke and sill orientation from pressurized magma chamber is often assessed from the analysis of the host rock principal stress orientations (Gudmundsson, 2006; Nakamura, 1977; Ode, 1957), as proposed by the early work of Anderson (1937). Anderson's formalism assumes that "central intrusions", such as cone-sheets, propagate as tensile fractures following principal stress trajectories. As discussed in several studies (Gerbault et al., 2012; Gerbault et al., 2018; Grosfils et al., 2015), and exemplified by our model results, this approach suffers severe limitations since it does not consider potential shear failure from the magmatic reservoir. Within the limitation of our cylindrical and finger-shaped geometry model, we show that shear failure may be a dominant mechanism. In this case, the orientation and distribution of the plastic strain (faults) is more likely to be controlled by the local heterogeneity of the system.

Despite a fundamental difference from the investigated length scales, our results are in good agreement with those of Currenti and Williams (2014); Gerbault et al. (2012); Gerbault et al. (2018); Minakov et al. (2018), which assess the initiation and orientation of "central intrusions" from a magmatic source. Minakov et al. (2018) investigated the elastoplastic response of a heterogeneous crust to explain the particular distribution of dyke swarms in the arctic region. Their work suggests that the presence of heterogeneity within the crust is a key factor to the development of shear-oriented fault patterns, which subsequently control the emplacement of dykes. Their approach is comparable to ours but applies to a much larger scale, where elastoplastic strain is directly interpreted as faulting. Currenti and Williams (2014); Gerbault et al. (2012); Gerbault et al. (2018), investigated km-scale failure patterns around magma chambers in the upper crust within the framework of elastoplastic deformations. These studies illustrate the complex shear failure patterns that may emerge in the overburden of a magma chamber resulting from the interplay between overpressure and the free surface. Finally, our results are in line with the models of Haug et al. (2018), Haug et al. (2017), Bertelsen et al. (2018) and Schmiedel et al. (2019), which showed how plastic shear damage zones induced by overpressurized intrusions can subsequently control the evolution and propagation of the intrusions along planes that are oblique to the principal stress trajectories.

5.3. Geophysical and geological implications

Similar to cylindrical and finger-shaped intrusions, dykes often display evidence of plastic strain in the process zone. Recent monitoring of dyke emplacement events in Iceland (Ágústsdóttir et al., 2016; White

et al., 2011) revealed that most earthquakes accommodating the propagation of the dykes are associated with shear failure subparallel to the propagation direction, and with almost no seismic component of tensile opening. The proposed interpretation of this atypical seismic signal is a combination of a first aseismic tensile opening of the host associated with a later phase of shear failure (Ágústsdóttir et al., 2016). The rupture length of the faults triggering the seismic signal (small-earthquake of magnitude < 2) can be estimated in the range of 100–200 m (Got et al., 2017; Wells and Coppersmith, 1994), which could well be within the process zone of the system. As illustrated by our study, fault development at the length scale of the intrusion process zone could largely be influenced by the local host heterogeneity. Addressing emplacement mechanism for dyke in rift zone is beyond the applicability of our model. However, our results present the importance of local heterogeneity in the development of the process zone in elastoplastic media, which is a framework that could motivate further development towards the study of complex deformation patterns observed in dyke systems.

5.4. Implications for borehole breakout

The geometry and the development of the plastic process zone modelled for finger intrusions in this study can potentially be apply to breakout processes observed along drilled boreholes. In this process, the original circular cross-section of the borehole develops into an elliptical shape, due to damage and rock failure of the walls. Based on a simple stress analysis, Zoback et al. (1985) linked the development of the damage zone with in-situ compressive stress regime exceeding the compression shear strength of the wall rocks, which results in damage growth in the direction of the minimum horizontal stress. It is noteworthy that the development of the damage zone in this process is well understood and documented to occur as shear failure of the walls (Meier et al., 2013; Zoback et al., 1985). One interesting results of our study is to show that the heterogeneity of the rock can facilitate and seed the development of the plastic strain along shear planes, as observed in borehole breakup, and potentially have an impact on the development of the process zone. Resolving the plastic strains induced by rock heterogeneity on centimetre to millimetre scale, as done in this study, may be relevant to assess the variability of borehole breakout patterns in wells drilled through successive sedimentary layers.

6. Conclusions

We have studied the development of the process zone associated with magma emplacement in a heterogeneous host. Our high resolution numerical models allowed us to investigate complex deformation patterns emerging from heterogeneities introduced in several spatial scales in the host rock. The following conclusions can be drawn from our results:

- Small variations in host rock properties (cohesion) can promote complex shear failure within a confined process zone around cylindrical conduits, including finger-shaped magmatic intrusions.
- Relatively “weak” variations (± 10%) of the host rock properties is sufficient to localize and partitioned the plastic deformation within the process zone. The presence of layers in sedimentary units may strongly guide the deformation resulting in a high level of strain partitioning within local units, as systematically observed within the Neuquén basins shales.
- The spatial extent of the process zone is estimated to be in the order of the intrusion thickness scale, which is the meter scale in our specific model setup of finger-shaped intrusion.
- Meter-scale outcrop observations may reveal the process zone deformation regime, which is dominated by the heterogeneity of the host.
- Heterogeneities with characteristic wavelength of 10 to 30% of the characteristic length scale of the intrusion seem to favour strain localization for a given load condition.

Acknowledgements

The authors acknowledge the reviewers (Eric Grosfils and anonymous) as well as the editor Philippe Agard for providing insightful reviews. This work was supported by the Research Council of Norway through the DIPS project (grant no. 240467). ØTH positions were funded by the Faculty of Mathematics and Natural Sciences at the University of Oslo. AS thanks M. Gerbault, A. Minakov, M. Wangen, and T. Duretz for discussions on various aspects of elastoplastic deformations.

Appendix A. Supplementary data

Supplementary data to this article can be found online at https://doi.org/10.1016/j.tecto.2019.05.016.

References

Abdelmalak, M.M., Mourgues, R., Galland, O., Bureau, D., 2012. Fracture Mode Analysis and Related Surface Deformation During Dyke Intrusion: Results From 2D Experimental Modelling: Earth and Planetary Science Letters. vol. 359. pp. 93–105.
Adamuszek, M., Dabrowski, M., Schmid, D.W., 2016. Folder: a numerical tool to simulate the development of structures in layered media. J. Struct. Geol. 84, 85–101.
Ágústsdóttir, T., Woods, J., Greenfield, T., Green, R.G., White, R.S., Winder, T., Brandsdóttir, B., Steinthórsson, S., Soosalu, H., 2016. Strike-slip faulting during the 2014 Bárðarbunga-Holuhraun dike intrusion, central Iceland. Geophys. Res. Lett. 43, 1495–1503.
Ambrose, J., 2014. Failure of Anisotropic Shales Under Triaxial Stress Conditions.
Anderson, E., 1937. Cone-sheets and ring-dykes: the dynamical explanation. Bull. Volcanol. 1, 35–40.
Baud, P., Schubnel, A., Wong, T.f., 2000. Dilatancy, compaction, and failure mode in Solnhofen limestone. Journal of Geophysical Research: Solid Earth 105, 19289–19303.
Bertelsen, H.S., Rogers, B.D., Galland, O., Dumazer, G., Abbana Bennani, A., 2018. Laboratory modelling of coeval brittle and ductile deformation during magma emplacement into viscoelastic rocks. Front. Earth Sci. 6. https://doi.org/10.3389/feart.2018.00199.
Bunger, A., Cruden, A., 2011. Modeling the growth of laccoliths and large mafic sills: role of magma body forces. Journal of Geophysical Research: Solid Earth 116 v.
Carrier, A., Got, J.L., Peltier, A., Ferrazzini, V., Staudacher, T., Kowalski, P., Boissier, P., 2015. A damage model for volcanic edifices: implications for edifice strength, magma pressure, and eruptive processes. Journal of Geophysical Research: Solid Earth 120, 567–583.
Chevallier, L., Gibson, L., Nhleko, L., Woodford, A., Nomquphu, W., Kippie, I., 2004. Hydrogeology of fractured-rock aquifers and related ecosystems within the Qoqodala dolerite ring and sill complex, Great Kei catchment, Eastern Cape. Water Res. Com., S. Afr 1238, 127.
Currenti, G., Williams, C.A., 2014. Numerical modeling of deformation and stress fields around a magma chamber: constraints on failure conditions and rheology. Phys. Earth Planet. Inter. 226, 14–27.
Dabrowski, M., Krotkiewski, M., Schmid, D., 2008. MILAMIN: MATLAB-based finite element method solver for large problems. Geochem. Geophys. Geosyst. 9.
de Souza Neto, E.A., Peric, D., Owen, D.R., 2011. Computational Methods for Plasticity: Theory and Applications. John Wiley & Sons.
Detournay, E., 2016. Mechanics of hydraulic fractures. Annu. Rev. Fluid Mech. 48, 311–339.
Galland, O., E. Holohan, B. v. W. de Vries, and S. Burchardt, 2018, Laboratory modelling of volcano plumbing systems: a review, *in* R. S. Breitkreuz C., ed., Physical Geology of Shallow Magmatic Systems. Advances in Volcanology, Springer, Cham.
Galland, O., Spacapan, J.B., Rabbel, O., Mair, K., Soto, F.G., Eiken, T., Schiuma, M., Leanza, H.A., 2019. Structure, emplacement mechanism and magma-flow significance of igneous fingers – implications for sill emplacement in sedimentary basins. J. Struct. Geol. https://doi.org/10.1016/j.jsg.2019.04.013.
Gerbault, M., Cappa, F., Hassani, R., 2012. Elasto-plastic and hydromechanical models of failure around an infinitely long magma chamber. Geochem. Geophys. Geosyst. 13.
Gerbault, M., Hassani, R., Novoa Lizama, C., Souche, A., 2018. Three-dimensional failure patterns around an inflating magmatic chamber. Geochem. Geophys. Geosyst. 19 (3), 749–771.
Got, J.L., Carrier, A., Marsan, D., Jouanne, F., Vogfjörd, K., Villemin, T., 2017. An analysis of the nonlinear magma-edifice coupling at Grimsvötn volcano (Iceland). Journal of Geophysical Research: Solid Earth 122, 826–843.
Got, J.-L., Amitrano, D., Stefanou, I., Brothelande, E., Peltier, A., 2019. Damage and strain localization around a pressurized shallow-level magma reservoir. Journal of Geophysical Research: Solid Earth 124, 1443–1458. https://doi.org/10.1029/2018JB016407.
Grosfils, E.B., 2007. Magma reservoir failure on the terrestrialplanets: assessing the

importance of gravitational loading in simple elastic models. J. Volcanol. Geotherm. Res. 166 (2), 47–75.
Grosfils, E.B., McGovern, P.J., Gregg, P.M., Galgana, G.A., Hurwitz, D.M., Long, S.M., Chestler, S.R., 2015. Elastic models of magma reservoir mechanics: a key tool for investigating planetary volcanism. Geol. Soc. Lond., Spec. Publ. 401, 239–267.
Gudmundsson, A., 2006. How local stresses control magma-chamber ruptures, dyke injections, and eruptions in composite volcanoes. Earth Sci. Rev. 79, 1–31.
Guldstrand, F., Burchardt, S., Hallot, E., Galland, O., 2017. Dynamics of surface deformation induced by dikes and cone sheets in a cohesive Coulomb brittle crust. Journal of Geophysical Research: Solid Earth 122, 8511–8524.
Haug, Ø.T., Galland, O., Souloumiac, P., Souche, A., Guldstrand, F., Schmiedel, T., 2017. Inelastic damage as a mechanical precursor for the emplacement of saucer-shaped intrusions. Geology 45, 1099–1102.
Haug, Ø., Galland, O., Souloumiac, P., Souche, A., Guldstrand, F., Schmiedel, T., Maillot, B., 2018. Shear versus tensile failure mechanisms induced by sill intrusions–Implications for emplacement of conical and saucer-shaped intrusions. Journal of Geophysical Research: Solid Earth 123 (5), 3430–3449.
Johnson, A.M., Pollard, D.D., 1973. Mechanics of growth of some laccolithic intrusions in the Henry Mountains, Utah, I: field observations, Gilbert's model, physical properties and flow of the magma. Tectonophysics 18, 261–309.
Kavanagh, J.L., Menand, T., Sparks, R.S.J., 2006. An experimental investigation of sill formation and propagation in layered elastic media. Earth Planet. Sci. Lett. 245, 799–813.
Keller, T., May, D.A., Kaus, B.J., 2013. Numerical modelling of magma dynamics coupled to tectonic deformation of lithosphere and crust. Geophys. J. Int. 195, 1406–1442.
Lister, J.R., Kerr, R.C., 1991. Fluid-mechanical models of crack propagation and their application to magma transport in dykes. Journal of Geophysical Research: Solid Earth 96, 10049–10077 v.
Maccaferri, F., Bonafede, M., Rivalta, E., 2011. A quantitative study of the mechanisms governing dike propagation, dike arrest and sill formation. J. Volcanol. Geotherm. Res. 208, 39–50.
Magee, C., Muirhead, J., Schofield, N., Walker, R., Galland, O., Holford, S., Spacapan, J., Jackson, C.A.-L., McCarthy, W., 2017. Structural Signatures of Igneous Sheet Intrusion Propagation.
Meier, T., Rybacki, E., Reinicke, A., Dresen, G., 2013. Influence of borehole diameter on the formation of borehole breakouts in black shale. Int. J. Rock Mech. Min. Sci. 62, 74–85.
Mériaux, C., Lister, J.R., Lyakhovsky, V., Agnon, A., 1999. Dyke propagation with distributed damage of the host rock. Earth Planet. Sci. Lett. 165, 177–185.
Michaut, C., 2011. Dynamics of magmatic intrusions in the upper crust: theory and applications to laccoliths on Earth and the Moon. Journal of Geophysical Research: Solid Earth 116 v.
Minakov, A., Yarushina, V., Faleide, J.I., Krupnova, N., Sakoulina, T., Dergunov, N., Glebovsky, V., 2018. Dyke emplacement and crustal structure within a continental large igneous province, northern Barents Sea. Geol. Soc. Lond., Spec. Publ. 460, 371–395.
Nakamura, K., 1977. Volcanoes as possible indicators of tectonic stress orientation—principle and proposal. J. Volcanol. Geotherm. Res. 2, 1–16.
Ode, H., 1957. Mechanical analysis of the dike pattern of the Spanish Peaks area, Colorado. Geol. Soc. Am. Bull. 68, 567–576.
Pollard, D.D., 1973. Derivation and evaluation of a mechanical model for sheet intrusions. Tectonophysics 19, 233–269.
Pollard, D., 1987. Elementary Fracture Mechanics Applied to the Structural Interpretation of Dykes, Mafic Dyke Swarms. vol. v. 34. Geological Association of Canada, pp. 5–24.
Pollard, D.D., Johnson, A.M., 1973. Mechanics of growth of some laccolithic intrusions in the Henry Mountains, Utah, II: bending and failure of overburden layers and sill formation. Tectonophysics 18, 311–354.
Pollard, D.D., Muller, O.H., Dockstader, D.R., 1975. The form and growth of fingered sheet intrusions. Geol. Soc. Am. Bull. 86, 351–363.
Rivalta, E., Taisne, B., Bunger, A., Katz, R., 2015. A review of mechanical models of dike propagation: schools of thought, results and future directions. Tectonophysics 638, 1–42.
Rodriguez Monreal, F., Villar, H.J., Baudino, R., Delpino, D., Zencich, S., 2009. Modeling an atypical petroleum system: a case study of hydrocarbon generation, migration and accumulation related to igneous intrusions in the Neuquén Basin, Argentina. Mar. Pet. Geol. 26, 590–605. https://doi.org/10.1016/j.marpetgeo.2009.01.005.
Rubin, A.M., 1993. Tensile fracture of rock at high confining pressure: implications for dike propagation. Journal of Geophysical Research: Solid Earth 98, 15919–15935 v.
Rubin, A.M., 1995. Propagation of magma-filled cracks. Annu. Rev. Earth Planet. Sci. 23, 287–336.
Rubin, A.M., Gillard, D., 1998. Dike-induced earthquakes: theoretical considerations. Journal of Geophysical Research: Solid Earth 103, 10017–10030.
Sammis, C.G., Julian, B.R., 1987. Fracture instabilities accompanying dike intrusion. Journal of Geophysical Research: Solid Earth 92, 2597–2605.
Scheibert, J., Galland, O., Hafver, A., 2017. Inelastic deformation during sill and laccolith emplacement: insights from an analytic elastoplastic model. Journal of Geophysical Research: Solid Earth 122, 923–945.
Schellart, W., 2000. Shear test results for cohesion and friction coefficients for different granular materials: scaling implications for their usage in analogue modelling. Tectonophysics 324, 1–16.
Schmiedel, T., Galland, O., Haug, Ø.T., Dumazer, G., Breitkreuz, C., 2019. Coulomb failure of Earth's brittle crust controls growth, emplacement and shapes of igneous sills, saucer-shaped sills and laccoliths. Earth Planet. Sci. Lett. 510, 161–172. https://doi.org/10.1016/j.epsl.2019.01.011.
Schofield, N., Stevenson, C., Reston, T., 2010. Magma fingers and host rock fluidization in the emplacement of sills. Geology 38, 63–66.
Senger, K., Millett, J., Planke, S., Ogata, K., Eide, C.H., Festøy, M., Galland, O., Jerram, D.A., 2017. Effects of Igneous Intrusions on the Petroleum System: A Review: First Break. vol. 35. pp. 47–56.
Sigmundsson, F., Hooper, A., Hreinsdóttir, S., Vogfjörd, K.S., Ófeigsson, B.G., Heimisson, E.R., Dumont, S., Parks, M., Spaans, K., Gudmundsson, G.B., 2015. Segmented lateral dyke growth in a rifting event at Bárðarbunga volcanic system, Iceland. Nature 517, 191.
Souche, A., 2018. Open-GeoNabla. https://github.com/albansouche/Open-GeoNablaZenodohttps://doi.org/10.5281/zenodo.1172193.
Spacapan, J.B., Galland, O., Leanza, H.A., Planke, S., 2017. Igneous sill and finger emplacement mechanism in shale-dominated formations: a field study at Cuesta del Chihuido, Neuquén Basin, Argentina. J. Geol. Soc. 174, 422–433.
Spacapan, J.B., Palma, J.O., Galland, O., Manceda, R., Rocha, E., 2018. Thermal impact of igneous sill-complexes on organic-rich formations and implications for petroleum systems: A case study in the northern Neuquén Basin, Argentina. Mar. Pet. Geol. 91, 519–531.
Townsend, M.R., Pollard, D.D., Smith, R.P., 2017. Mechanical models for dikes: a third school of thought. Tectonophysics 703, 98–118.
Wells, D.L., Coppersmith, K.J., 1994. New Empirical Relationships Among Magnitude, Rupture Length, Rupture Width, Rupture Area, and Surface Displacement. vol. 84. Bulletin of the seismological Society of America, pp. 974–1002.
White, R.S., Drew, J., Martens, H.R., Key, J., Soosalu, H., Jakobsdóttir, S.S., 2011. Dynamics of dyke intrusion in the mid-crust of Iceland. Earth Planet. Sci. Lett. 304, 300–312.
Yarushina, V., Dabrowski, M., Podladchikov, Y., 2010. An analytical benchmark with combined pressure and shear loading for elastoplastic numerical models. Geochem. Geophys. Geosyst. 11.
Zoback, M.D., Moos, D., Mastin, L., Anderson, R.N., 1985. Well bore breakouts and in situ stress. Journal of Geophysical Research: Solid Earth 90, 5523–5530.